Visual
Abstract

Failure analysis of compressed earth block using numerical plastic damage model

Bouhiyadi Samir, Souinida Laidi, El hassouani Youssef
Moulay Ismail University of Meknès, Laboratory of Engineering Sciences and Techniques, FST Errachidia, BP 509, Boutalamine, 52000, Errachidia-Morocco
samir.bouhiyadi@gmail.com, laidi_sou@yahoo.fr, y.elhassouani@fste.umi.ac.ma

ABSTRACT. In the last decade, several studies have been introduced to the development and use of compressed earth blocks in green building construction. Studying the evaluation of existing cracks in construction buildings by these blocks is an important industrial and safety subject in recent research. This objective opens a new field in building construction where we describe the mechanical behavior of compressed earth solid blocks. In addition, we offer a solution to rupture damages presented by the propagation of masonry cracks. This paper aims to explore a numerical study using ABAQUS where we analyze the mechanical properties of this block. We started by investigating the elastic phase for this material and it has been generalized to a study in the plastic regime and rupture for the studied block. The different results of simulation shows that macro-cracks generate in the extremities and intersect each other horizontally and/or propagate towards the upper part of the block in a way that is practically parallel to the application of the compression test force.

KEYWORDS. Earth construction; Green building; Rupture; Inelastic strain; Compression damage; Crack propagation.

OPEN ACCESS

INTRODUCTION

Over the past few years, several sectors of global industry have attached great importance to reducing energy consumption, namely, in building construction, for a sustainable and ecological future [1]. Moreover, the World Bank estimates that three billion people worldwide need 300 million new homes by 2030 [2]. In Morocco, this main objective is supported by an energy efficiency strategy and passive construction. In this respect, a key investigation of this goal is relevant to the recent demand for the green building based on raw earth construction materials.

Green building, especially based on raw earth, has environmental, economic, and comfort advantages. Indeed, several manufacturing methods have been developed over the years and devoted themselves to a variety of uses. Generally, humanity has benefited from the development of a wide variety of production techniques. Today, we are witnessing a growing return to raw earth construction, supported by scientific research [3]. Moreover, raw earth is a very common

material in local housing construction. Soil is everywhere and therefore accessible to the population [4]. Thus, a simple natural treatment, with the addition of appropriate aggregates and additives, transforms the extracted soil into a homogeneous and manageable soil that can be further prepared, mechanically shaped, and properly dried. This mixture presents the treated soil as a strong and durable building material [5]. The strength of the soil is due to the cohesion of its ingredients and the clay fraction that acts as a natural binder.

The duration of a building on raw earth is very often linked to its construction techniques. Currently, these local materials, in their non-stabilized form, present some defects such as the lack of mechanical strength, systematic cracking due to shrinkage, and high sensitivity to water [5]. In the light of this problem, we are interested in testing, improving, and developing local building materials. These materials are developed using modern techniques while optimizing the mechanical performance and increasing the life span of the blocks.

The environmental and sustainability quality of raw earth has also driven to design various construction techniques. In some cases, the earth is amended with fibers, mainly vegetal, to limit shrinkage cracking or increase its insulating properties. We can distinguish between monolithic walls and those made of bricks. The best-known techniques are shown in the earthen construction wheel presented by H. Guillaud et H. Houben (2006) [6]. The main methods illustrated in the wheel are non-standardized with limitations in use, due to the lack of adequate experimental data on the structural behavior properties of buildings.

These methods present limitations to the practice of green building. Firstly, in the world, we have a great heterogeneity in the composition of the raw earth (sandy environmental soil, gravelly soil, laterite soil, and clay soil) [7]. Secondly, the soil differs from one area to another; therefore, soil analysis is necessary to identify which one is suitable for block making [8]. Thirdly, there are the delicate conditions of stabilization. Indeed, Winterkorm [9] has shown that the main objective of raw earth stabilization is to obtain the best mechanical characteristics of the soil. Finally, at present, the lack of calculation and numerical control tools for the construction and stabilization techniques account for its specificities and no investigated use characteristics.

The aim of this study is to illustrate the empirical knowledge of raw earth as a green building method. However, if we have developed several methods, the study will be a costly solution, and if we have selected only one concept, it will be risky. Therefore, the reliability of the raw earth product, in the early stages of design, is to detail recent research, which becomes an advantage for further validation of information.

According to Ben Ayed et al [1], one of the modern earth construction techniques is the Interlocking Stabilized Earth Block. The use of this technique is suitable for high environmental quality because the process uses a material that does not require much processing energy. In addition to this, the earth blocks do not require any treatment before being recycled. Besides, recent research on compressed earth blocks shows that compressive strength is an important parameter for building design [10]. Therefore, there has been a major interest in studying the mechanical behavior and durability related to the construction problems of compressed earth blocks.

This paper focuses on verifying the suitability of compressed earth blocks to be used in dry stacked walls. In our current life, there are several types. Thus, to study several structures is an expensive solution. Our objective is to identify the behavior of a single block and to understand the most critical areas to be stabilized. As mentioned before, it is obvious to study the mechanical behavior of compressed earth blocks. Before realizing this vision, we decided to describe the compressed earth block in a general context, then we chose a solid form, to start the procedure of simulating the compressive strength of this block. At this stage, a comparative study of the experimental measurements elaborated by Ben Ayed et al [1] and our numerical simulation was done. The mechanical properties of the compressed earth block in an elastic phase were simulated. This study will be useful in avoiding the cracks in masonry based on solid compressed earth blocks. Indeed, we have enhanced the modeling by determining the plastic and rupture damage properties of the compressed earth blocks, namely the inelastic deformations, and the damage coefficients resulting from compression and tensile of the studied block. Finally, a numerical simulation of the crack propagation was made.

DESCRIPTION OF THE COMPRESSED EARTH BLOCKS

Compressed earth blocks are small masonry units mainly made of raw earth, which are generally parallelepiped in shape, and common dimensions differ from one casting to another, and the drying method used [11]. Compressed earth blocks have several main criteria to be considered before being used in building construction. On the one hand, the geometry is defined by the nominal dimensions L (length) × W (width) × H (height), and on the other hand, the compressed earth block masonry, which is a structure of small elements piled up together and constituting a building block that has a compressive strength. Therefore, to have a better characterization of the mechanical properties

of compressed earth blocks, it is necessary to test them in the condition in which the earth masonry unit is manufactured [1].

The tradition of the production of compressed earth blocks has adopted mainly a parallelepiped shape and dimensions compatible with a mass of 6 to 8 kg. In this work, we propose to study the mechanical response of a compressed earth block whose geometries have the following dimensions $240 \times 220 \times 97$ mm^3 (L × W × H) [1].

Earth block masonry arrangements in the literature include stacking bonds, running bonds, and Flemish bonds (Fig. 1). The influence of the block arrangement on the compressive performance of the masonry is mainly reflected in the weakening effect of the mortar joints on the integrity of the masonry [11].

For our study, we simulated the solid blocks of compressed earth in the mortarless masonry layout type (Fig. 1a). This suggestion is the solution tested in the experimental trials conducted by Ben Ayed et al [1]. From this pile-up apparatus, in (Fig. 2), we have developed a numerical model of real conditions applied to the studied block. The vertical compression test is implemented by two opposing pressures on the contact faces between successive blocks. The block is designed to support vertical stress approximately 20 levels higher than the average stress under service conditions. This average stress can be as low as 0.2 MPa in a single-storey structure. South African norms (SANS 10164, 1996) recommend a minimum strength of 3 MPa for blocks and the British norms (BS 5628, 1978) recommend a minimum strength of 2.8 MPa [8]. Therefore, for our study, we have chosen a vertical pressure higher than the two norms mentioned above. This stress is equal to 5.68 MPa. This is equivalent to a vertical concentric force of 300 kN on an area of 220×240 mm^2 [13].

The physical properties of the compressed earth blocks used in this work were collected from the study presented by Ben Ayed et al [1]. These researchers have executed uniaxial compression tests. All the samples were produced by SOIB company which is a company in Tunisia. The stabilized soil for the SOIB blocks combines two high-quality materials. The first material is a local red soil based on the laterite, which was dried with ambient air, and it was sifted with a sieve of 8 mm. The second material is ordinary Portland cement with a percentage of 8%. The stabilized local material was mixed and hydraulically compacted in a machine based on the "HYDROFORM" concept under a pressure of 12 MPa. The main objective of soil compaction is to increase the density and strength of the soil and to reduce its porosity and water sensitivity. In addition, the prepared blocks are stacked and cured for 7 days under a cover.
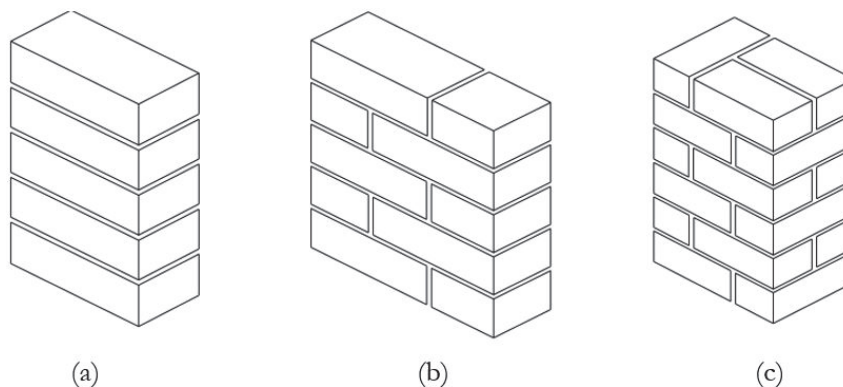
Figure 1: Layout of earthen blocks in different masonry: (a) Stacking bond; (b) Running bond; (c) Flemish bond [12].

FINITE ELEMENT ANALYSIS (F.E.M.) OF MECHANICAL CHARACTERIZATION TESTS OF PRE-SELECTED BLOCKS

T he compressed earth block was manipulated numerically as part of a macro-modeling strategy. It was therefore treated as a homogeneous solid and no distinction was made between the masonry elements. Thus, the joint between blocks is made without mortar (mechanical locking). Therefore, the distribution of the vertical pressure 5.68 MPa is homogeneous on the contact surface between blocks.

Ben Ayed et al [1] carried out an experimental study consisting of testing different block arrangements (Fig. 3): a test on a single solid block, a test on two interlocking blocks, and a test on three interlocking blocks.

The samples were tested by a uniaxial compression experiment using a hydraulic press. Ben Ayed et al [1] proposed 5 homogeneous samples to obtain a good average of the measured parameters. The upper and lower surfaces of the blocks were surfaced to achieve a total adhesion between the block and the upper and lower platens of the machine. The uniaxial compression test is realized at a rate of constant displacement of the piston which is 0.02 mm/s. The displacement

imposed on the lower platen and the associated load are automatically recorded. Curves (Fig. 13) in the paper presents the experimental results of the stress and strain of the 5 samples. The vertical compression stress is obtained by dividing the measured force F by the area $S = 220 \times 240$ of the block in contact with the platen. Thus, the vertical deformation along the axis of the applied load is equal to the vertical displacement divided by the height. Ben Ayed et al [1] proposed 3 heights for each case of study. For our case, of a single block, the deformation is calculated for the height of 97 mm.

The compression test was carried out by applying the experimental data (Tab. 1). The superior plate does not exceed a vertical displacement of 0.29 mm in the direction of the vertical compression force, and the latter attained a value of $F_{max} = 300 kN$. Thus, the behavior of the blocks is considered elastic-linear because the study is based on the elastic phase in the first place.
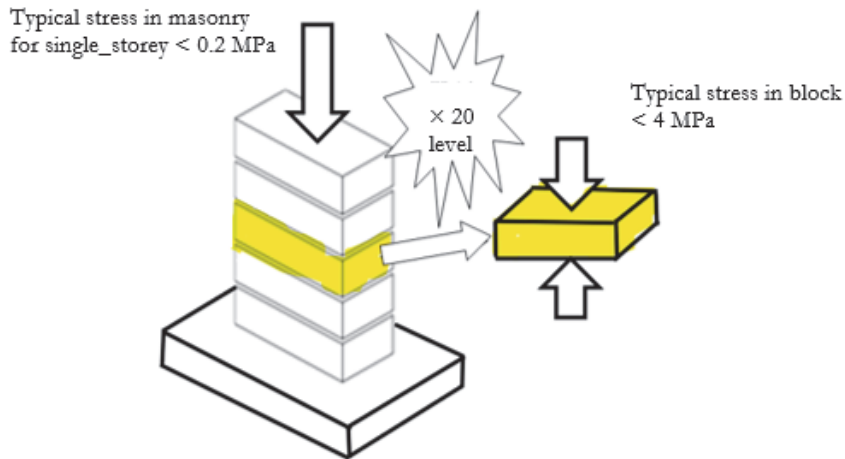
Figure 2: Average loading on a Layout of earthen blocks in Stacking bond masonry.
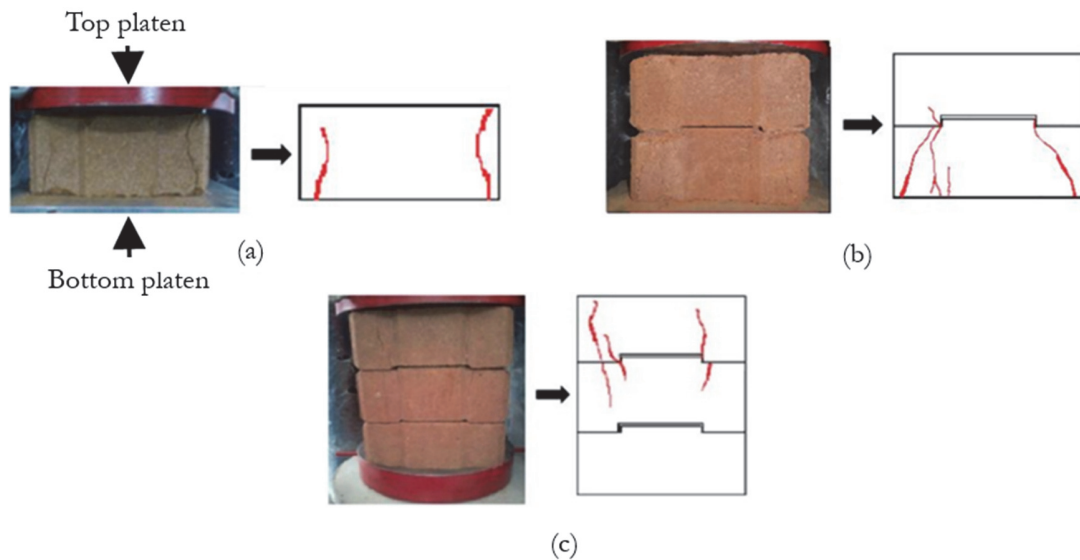
Figure 3: Compression tests and cracking pattern for: (a) one block, (b) two, and (c) three interlocking blocks [1].

Vertical displacement mm	Concentric force kN	Coefficient of tangential behavior	Young's modulus MPa	Poisson's ratio	Density kg/m³
0.29	300	0.7	1700	0.2	1950

Table 1: The Data of the simple compression test simulation.

The basic behavioral relationship (linear elasticity) between the deformations and stresses of the compressed earth block is written:

$$\sigma = D^{el} \times \varepsilon^{el} \tag{1}$$

with

σ : is the total constraint;

D^{el} : is the fourth order elasticity tensor or Hooke tensor;

ε^{el} : is the total elastic deformation.

We have chosen the simple form of linear elasticity; we have considered that the block behaves in the isotropic case. Then, the stress-strain relationship is given by the Eqn. (2).

$$\begin{Bmatrix} \varepsilon_{11} \\ \varepsilon_{22} \\ \varepsilon_{33} \\ \varepsilon_{12} \\ \varepsilon_{13} \\ \varepsilon_{23} \end{Bmatrix} = \begin{bmatrix} \tfrac{1}{E} & -\tfrac{\nu}{E} & -\tfrac{\nu}{E} & 0 & 0 & 0 \\ \tfrac{1}{E} & \tfrac{1}{E} & -\tfrac{\nu}{E} & 0 & 0 & 0 \\ -\tfrac{\nu}{E} & -\tfrac{\nu}{E} & \tfrac{1}{E} & 0 & 0 & 0 \\ 0 & 0 & 0 & \tfrac{1}{G} & 0 & 0 \\ 0 & 0 & 0 & 0 & \tfrac{1}{G} & 0 \\ 0 & 0 & 0 & 0 & 0 & \tfrac{1}{G} \end{bmatrix} \times \begin{Bmatrix} \sigma_{11} \\ \sigma_{22} \\ \sigma_{33} \\ \sigma_{12} \\ \sigma_{13} \\ \sigma_{23} \end{Bmatrix} \tag{2}$$

The Young's modulus E was chosen from experimental results obtained on a single solid block: $E = 1700 MPa$. Poisson's ratio is equal to 0.2 as suggested by B.V. Venkatarama Reddy [15] and the predefined density is equal, according to the literature, to $\rho = 1950\,{}^{kg}\!/_{m^3}$ [16].

This paper treats the numerical simulation of a single block of compressed earth under the action of a vertical compression load (Fig. 4a). This loading is generated by the condition that the block is condemned between two other blocks. Indeed, Ben Ayed et al [1] presented the contact between the plates, upper and lower, and the block by a tangential coefficient equal to 0.7. This value is measured by the experimental protocol (Fig. 4c).

Fig. 4b represents the ratio $\tan(\varphi) = \dfrac{T}{N}$ between the friction force T that resists the movement of two contacting surfaces and the normal force N that presses the two surfaces together. To identify this Coulomb friction coefficient $\mu = \tan(\varphi)$, Ben Ayed et al [1] have realized a compression test on samples (100 x 75 x 220 mm³) (Fig. 4c). These samples were cut into two portions according to the different angles α (Fig. 4c) between 10° and 45° with a step of 5°. Theoretically, if the two portions are rigid with perfect Coulomb friction between them, the compression test with a cutting angle α will give exactly a Coulomb criterion with a friction angle $\varphi = \alpha_1$ Starting from $\alpha = 0$ and increasing α for each test, angle α_1 corresponds to the first observed slip. This is demonstrated by considering Eqns. (3, 4, and 5) given by the projection of the compressive load N onto the slip surface $S_g = \dfrac{S}{\cos(\alpha)}$ where $S = 75 \times 100\,mm^2$.

$$\sigma_n = \frac{N}{S}\cos^2(\alpha) \tag{3}$$

$$\tau = \frac{N}{S} \times \sin(\alpha) \times \cos(\alpha) \tag{4}$$

$$\tau = \tan(\alpha) \times \sigma_n \tag{5}$$

In our case, the blocks are quasi-fragile under compressive loading. Indeed, Fig. 5 shows that even if cracks are not observed, a slip is noted above $\alpha_1 = \varphi = 35°$; it is observed for a load $N = 13.7 kN$. At the same time, a mixed failure scenario with slip and separation of the two parts was observed between $\alpha = 30°$ and $\alpha = 10°$. The Coulomb friction

criterion considered is the envelope curve of the experimental criterion for angles less than $\alpha_1 = \varphi = 35°$. Therefore, the coefficient of friction between blocks is equal to $\tan(\varphi) = \tan 35° = 0.7$. This Coulomb friction criterion is considered in our work as a surface-to-surface contact property.
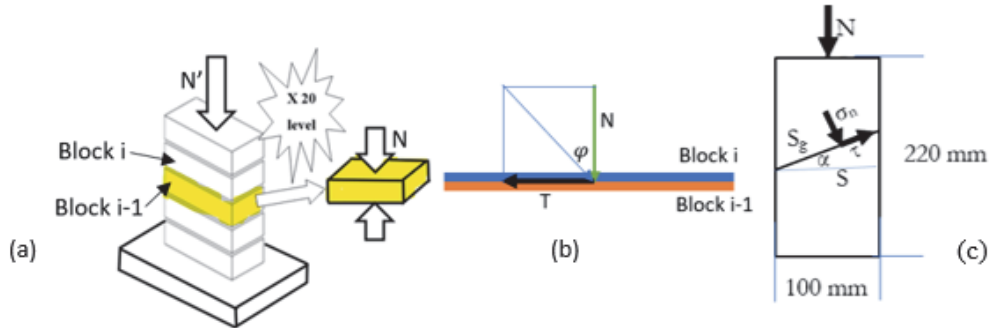
Figure 4: Theoretical modeling of the internal friction angle between compressed earth blocks.
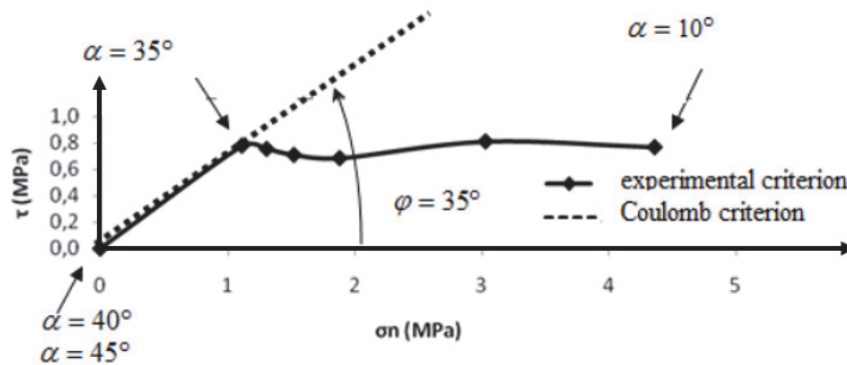
Figure 5: Tangential and normal stresses at failure (failure criterion)[1].

During our work, we proposed a square shell plate (300×300 mm²) to present the top and bottom platen of the compression test. Its model is a square shell without thickness so the force distribution will be homogeneous on the whole plate and the calculation time will be reduced. Moreover, ABAQUS does not need to have the shell material and the transfer of forces will be direct between the nodes of the plate and the top and bottom face of the block.

To successfully simulate the elastic behavior of the solid block, according to the predefined compression test data, we have carried out a numerical pre-simulation in four categories: a macroscopic simulation (Fig. 6a) with a coarse mesh, of type: linear hexagonal-structured C3D8R, under a number (10752 elements). A second fine simulation (Fig. 6b) of the type: (always a linear hexagonal-structured C3D8R mesh but finer than the Fig. 6a with a number of 42240 elements). A third simulation (Fig. 6c) is finer than the last two types: linear hexagonal-structured C3D8R and with 64064 elements. A fourth refinement (Fig. 6d) of type: linear hexagonal-structured C3D8R with 80640 elements.

The choice of mesh size is a key issue in finite element simulations: the finer the mesh size is, the less it contributes to the deviations between simulation and reality. However, we can observe in (Figs. 6 and 7) that the refinement of the mesh contributes to a convergence around the same values of the distribution of the von-Mises stress along the XY plane at node 69. That is to say, for optimizing the ratio between the precision of the results and the cost of the simulation, we have chosen the mesh (type: linear hexagonal-structured C3D8R and with 80640 elements).

In Fig. 8a, we observe a concentration of stress at the 4 extremities of the underside face of the block. In Figs. 8b and 8c, we notice a maximum tensile displacement at the other ends of the block on the upper side face. This will lead us to define a hypothesis that the block will start to crack from the articulation point at the bottom extremities upward till where a maximal moment is in front of it in the top (Fig. 8). This hypothesis is also proposed by Ben Ayed et al [1]; where they said that the block manifests itself by vertical cracks when subjected to vertical compression loading. Therefore, we

grant a predictive-qualitative similarity between the crack propagation in the experimental test (Fig. 3a) and that of our numerical simulation.

The von-Mises stress distribution (S, Mises) in Fig. 9 of the block shows us that the stresses in the sidewalls are greater than in the core. So, we have made a hypothesis that the first deformation is generated at the sides of the block and not in the core. Therefore, no visualization of rupture at the sides of the compressed earth block shows us a good resistance at the core of the block.

To compare the unidirectional stresses applied to the block, we captured the six images of the directional stresses in Fig. 10. The maximum unidirectional stress is well recorded along the Y-axis with a value of $(S_{22,max} = 10.04\,MPa)$. Also, we can observe that the 4 edges of the block have a high concentration of stress in all directions, so the stress is high on the contact surface with the bottom plate and reduces in the direction of the upper plate. This remark is in accordance with the above-mentioned hypothesis which says that the predicted crack propagation is generated at the 4 bottom corner points towards the other corner points at the top in an almost vertical way.

Fig. 11 shows the curves of the vertical strain ε_{22} and the vertical stress applied to the plate from the experimental tests performed by Ben Ayed et al [1] and for our numerical simulation. Before comparing the curves, it should be mentioned that the comparison is discussed from the elastic zone with maximum vertical stress reaching 40% of the ultimate stress [17]. However, the minimum ultimate stress of the 5 experimental tests is 11.45 MPa corresponds to test 1-5 then the maximum elastic study limit of comparison is $\sigma_{max} = 4.58\,MPa$. From the curves in Fig. 11, we can see that the simulation and experimental results in the elastic regime are almost the same for the tests except test 1-1.
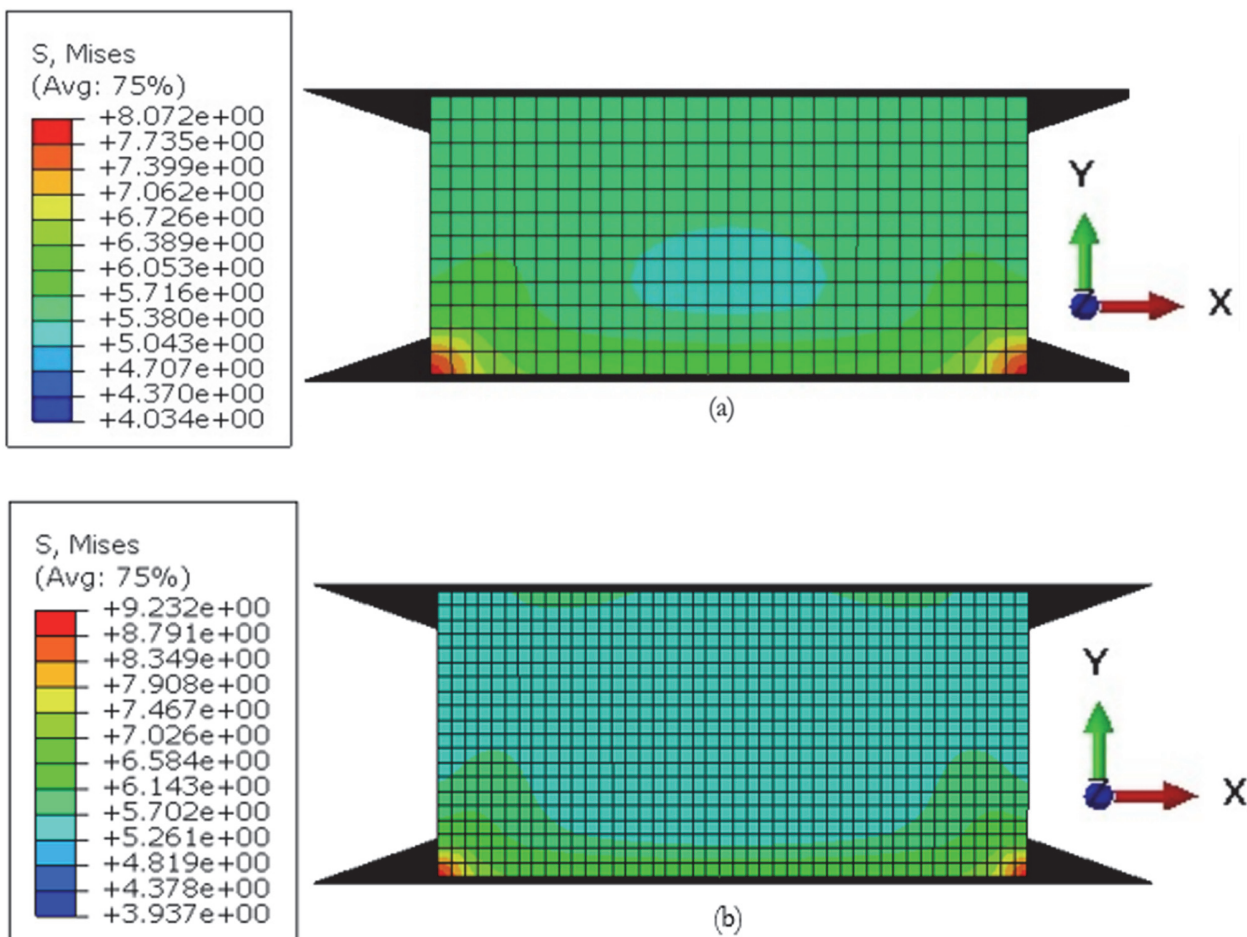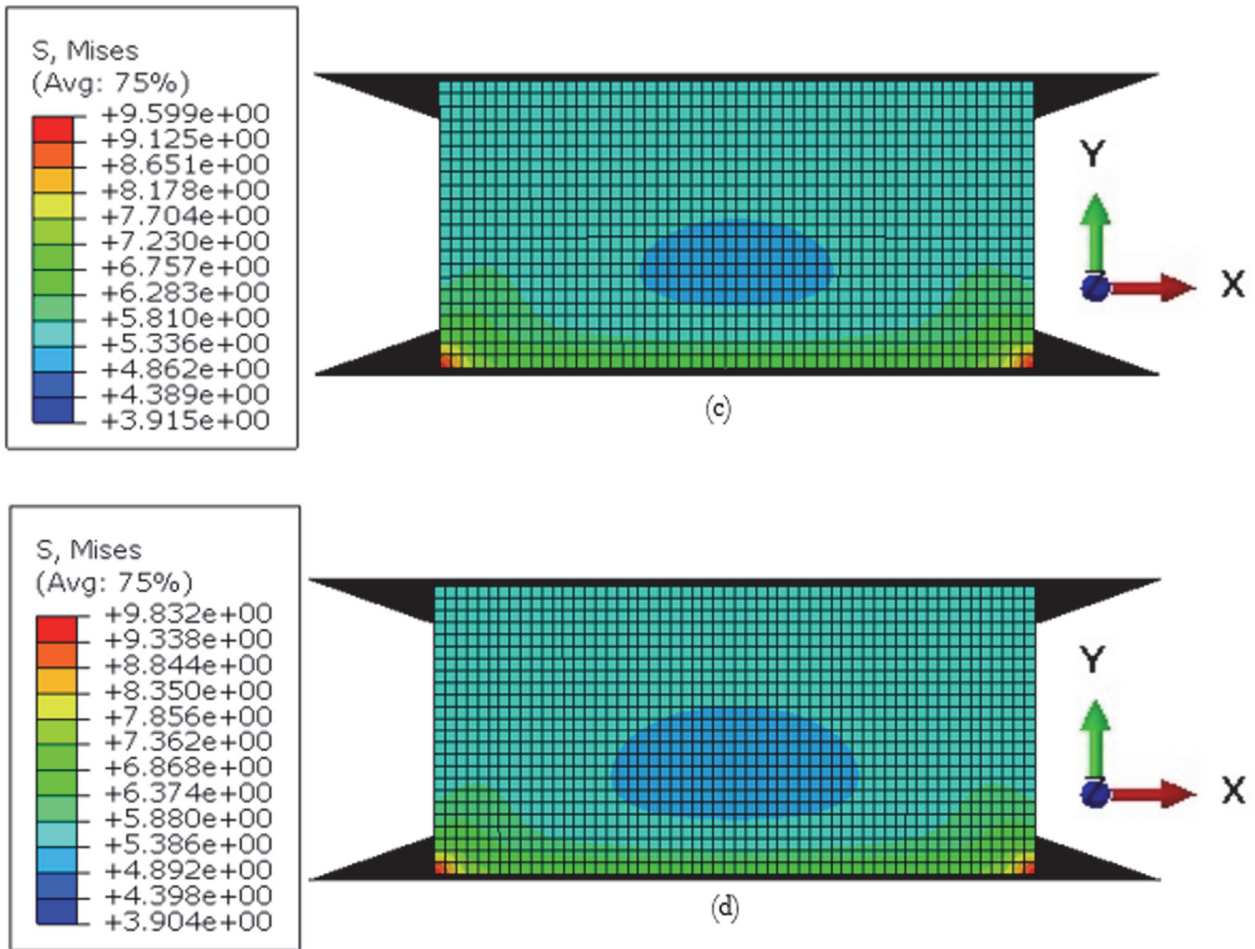
Figure 6: The von-Mises stress distribution of the solid block by compression test in the XY plane according to the mesh.
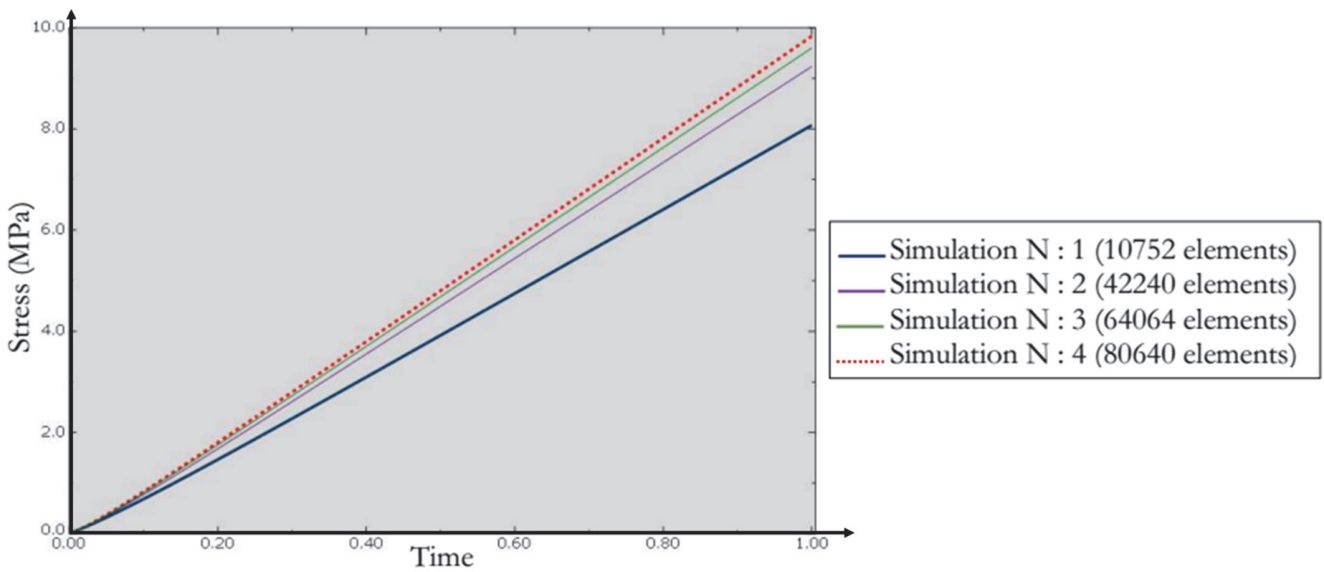
Figure 7: The distribution of the von-Mises stress (MPa) in the XY plane for the four meshes in node 69.
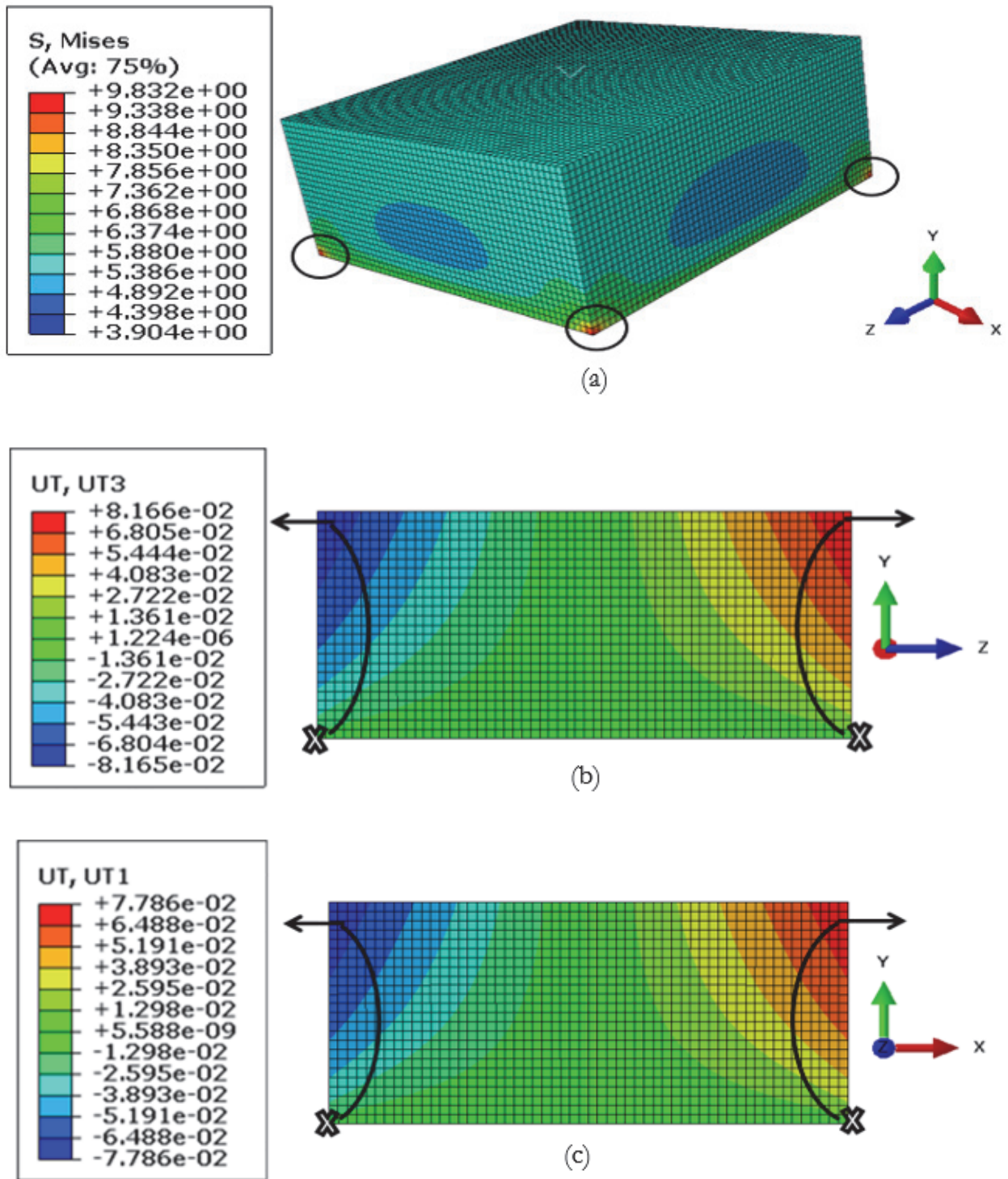
Figure 8: (a) The von-Mises stress, (b) Uniaxial displacements U_{T3}, (c) Uniaxial displacements U_{T1} in elastic simulation.
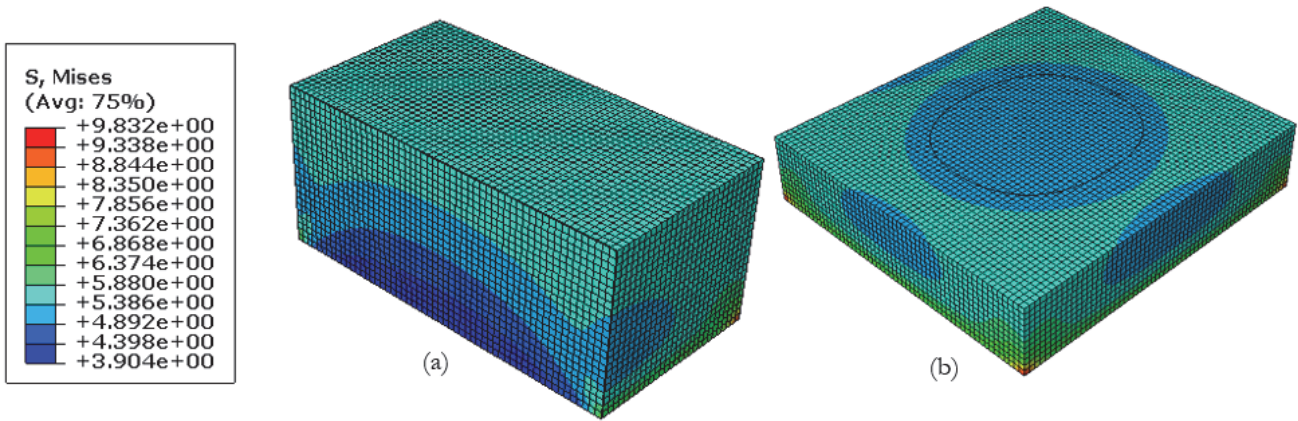
Figure 9: Two simple cuts along the XY (a) and XZ (b) plane of the von stress distribution put on the solid block.
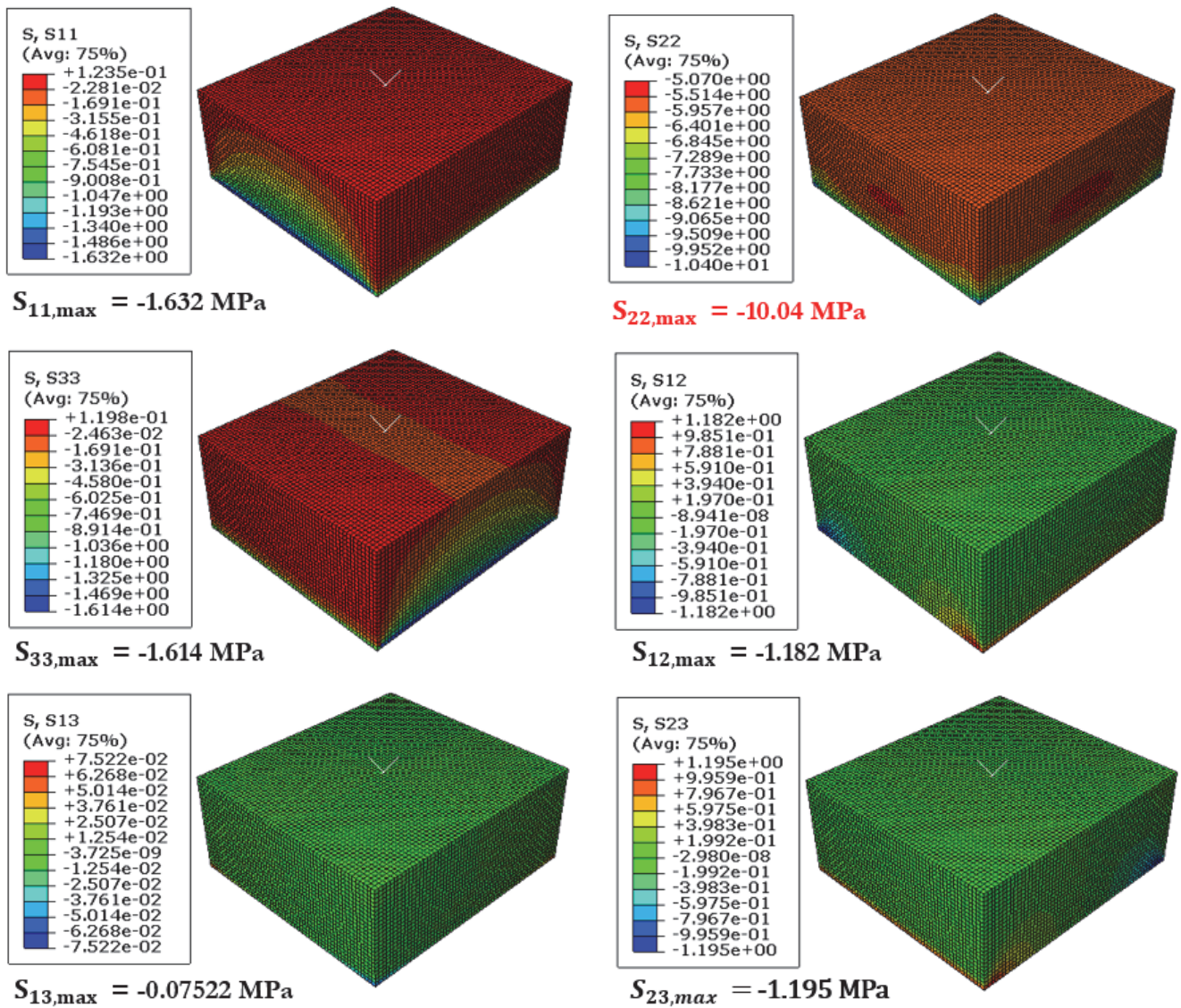
Figure 10: The distribution of the stresses in the selected block.
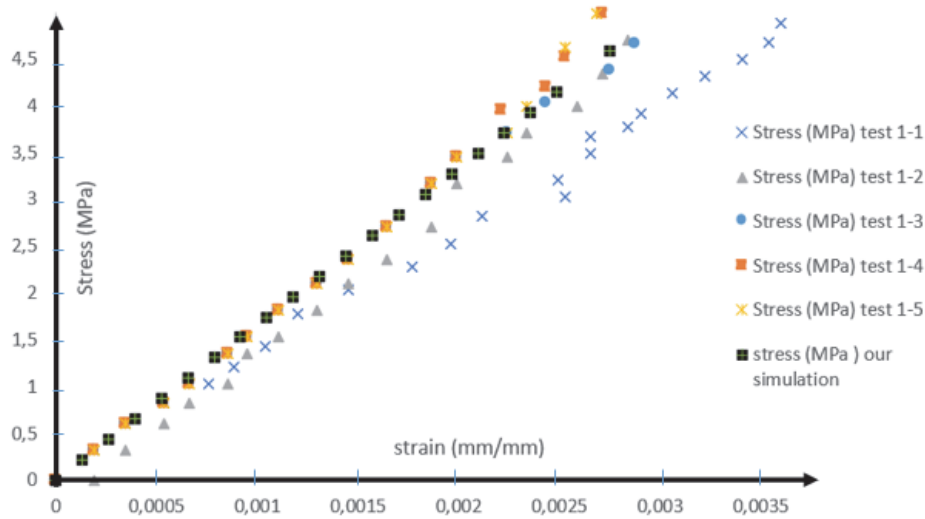
Figure 11: A comparison between the result of the simulation and the experimental compression test.

PLASTIC AND RUPTURE DAMAGE PROPERTIES OF COMPRESSED EARTH BLOCKS

The plasticity model of a damaged block on ABAQUS, uses the concepts of isotropic damaged elasticity in combination with isotropic plasticity in tension and compression, to represent the inelastic behavior of the block. The two main rupture mechanisms are assumed to be:
– Tensile cracking;
– Compressive crushing of the material.
The plastic damage model on ABAQUS is based on the models proposed by Lubliner et al (1989) and Lee and Fenves (1998) [18]. The model is described in the rest of this section. An overview of the main ingredients of the model is given first, followed by a more detailed discussion of the different aspects of the constitutive model.

Strain rate decomposition
Additive strain rate decomposition is assumed for the velocity independent model [14]:

$$(\varepsilon^* = \varepsilon^{*el} + \varepsilon^{*pl}) \tag{6}$$

with:

ε^* : the total strain rate;
ε^{*el} : the deformation rate of the elastic phase;
ε^{*pl} : the strain rate of the plastic phase.

Stress-strain relationship
The stress-strain relationship is governed by the damaged scalar elasticity [14,18]:

$$\sigma = (1-d)D_0^{el} : (\varepsilon - \varepsilon^{pl}) = D^{el} : (\varepsilon - \varepsilon^{pl}) \tag{7}$$

where

D_0^{el} : is the initial (undamaged) elastic stiffness of the material;

D^{el} : is the degraded elastic stiffness.

In Fig. 12, the elastic phase is linear up to the value of the initial yield which corresponds to 40% of the ultimate compressive stress $f_{cm} = \sigma_u$. According to Hashim et al [17], the 40% ratio is essential to define Young's modulus, which

characterizes the behavior of the compressed earth block in the elastic phase 1 (Fig. 12). In the plastic regime, the response is generally characterized by strain hardening phase 2 (Fig. 12) followed by a softening by deformation beyond the ultimate strength phase 3 (Fig. 12).

To determine the inelastic deformation of the point j of the "stress-strain" curve, it is necessary to draw the line parallel to the slope of the elastic phase and passing through the point j. The intersection of this line with the strain axis is the point of inelastic deformation in compression.

To get the plastic deformation in compression we use the empirical equation below:

We have

$$\varepsilon_{c,j} = \varepsilon_{c,j}^{in} + \frac{\sigma_{c,j}}{E_c} \tag{8}$$

and

$$\varepsilon_{c,j}^{pl} = \varepsilon_{c,j} - \frac{\sigma_{c,j}}{E_c(1-d_c)} \tag{9}$$

Then

$$\varepsilon_{c,j}^{pl} - \varepsilon_{c,j} - \frac{\sigma_{c,j}}{E_c} \times \frac{d_c}{1-d_c} \tag{10}$$

or [17]

$$d_c = 1 - \frac{\sigma_{c,j}}{\sigma_u} \tag{11}$$

So

$$\varepsilon_{c,j}^{pl} = \varepsilon_{c,j}^{in} - \frac{\sigma_{c,j}}{E_c} \times (\frac{\sigma_u}{\sigma_{c,j}} - 1) \tag{12}$$
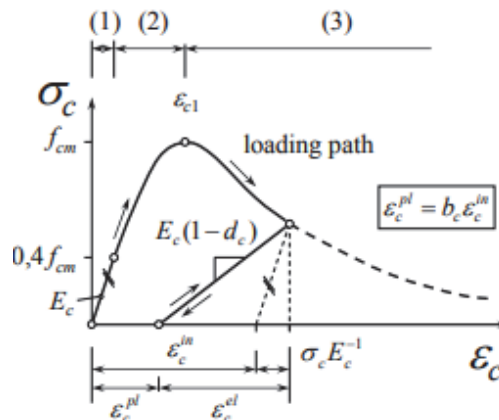
Figure 12: Stress-strain relation for compressive loading [19].

In Fig. 13, the last 4 stress-strain curves of compressed earth block solicited to a uniaxial load in compression present Young's modulus almost equal to 1700 MPa which is the initial proposal of our simulation, then a comparison between the experiment and the simulation must be between one of these tests. For our case, we choose the test 1-5. This curve presents the minimum ultimate stress ($\sigma_{cu,min} = 11.45 MPa$) compared to the selected tests.

The principal properties of the simple compression behavior of the block in test 1-5 are:

−   Young's modulus: it is the slope of the elastic part in the area $[0; 0.4 \times \sigma_{cu}]$ [17]:

$$E_0 = \frac{4.58}{0.0027} = 1696.29 MPa$$

−   The ultimate strength: $(\sigma_{cu,\min} = 11.45 MPa)$;

− ε^{in}: inelastic strain equivalent to compression at rupture is $\varepsilon^{in} = 0.0093$;

−   Damage factor d_c in rupture:

We have $d_c = 1 - \dfrac{\sigma_{c,j}}{\sigma_u}$ according to Hachim and al [17], Whatever the point j of the test curve 1-5 in Fig. 13.

Thus, the damage at rupture is:

$$d_{c,r} = 1 - \frac{10.8}{11.45} = 0.056$$

− $\varepsilon^{pl,j}$: the plastic strain equivalent to compression is :
    We have

$$\varepsilon_j^{pl} = \varepsilon_j^{in} - \frac{\sigma_{c,j}}{E_c} \times (\frac{\sigma_u}{\sigma_{c,j}} - 1)$$

Thus

$$\varepsilon_r^{pl} = 0.0093 - \frac{10.8}{1696.29} \times (\frac{11.45}{10.8} - 1) = 0.00891$$

−   The coefficient b_c with:

$$\varepsilon^{pl} = b_c \times \varepsilon^{in} \tag{13}$$

Therefore

$$b_c = \frac{\varepsilon^{pl}}{\varepsilon^{in}} = \frac{0.0089}{0.0093} = 0.956$$

− ε^{el}: the elastic strain equivalent to compression,
    We have

$$\varepsilon^{el} = \varepsilon_c - \varepsilon^{pl} \tag{14}$$

Thus

$$\varepsilon^{el,r} = 0.0156 - 0.00891 = 0.00669$$

The determination of material behavior laws is very important in numerical modelling. Thus, most soil materials are in the category of no associated materials, and their behavior is more complex [20]. In addition, the plastic and rupture damage properties of compressed soil blocks have been attributed to defining the compressive behavior, tensile behavior, and plasticity parameters, including the dilation angle, eccentricity, ratio f_{b0}/f_{c0}, K_0 value, and viscosity [21]. The strains, which result from the uniaxial compression of test 1-5 are presented in Fig. 13.

Typical methods treating soils undergoing a plastic flow direction that is not orthogonal to the flow surface generate two potential functions: a yield function that bounds the plasticity zone, and the flow potential that defines the plastic flow direction [21]. The use of these two potentials to describe soils breaks the framework of orthogonality between stress and plastic deformation, which is a classical property in solid mechanics.

Fig. 14 shows a non-associated Drucker-Prager as a classical model that describes the relations of stress and plastic strain rate that can be expressed by a constitutive Drucker-Prager cone. This curve consists of the hydrostatic part and the deviatoric part. The expansion angle factor controls the amount of volumetric plastic deformation developed. Dilatancy is a particular property of soils. Thus, after the model enters a plastic phase, the associated flow rule leads to a non-negligible volume expansion [21].
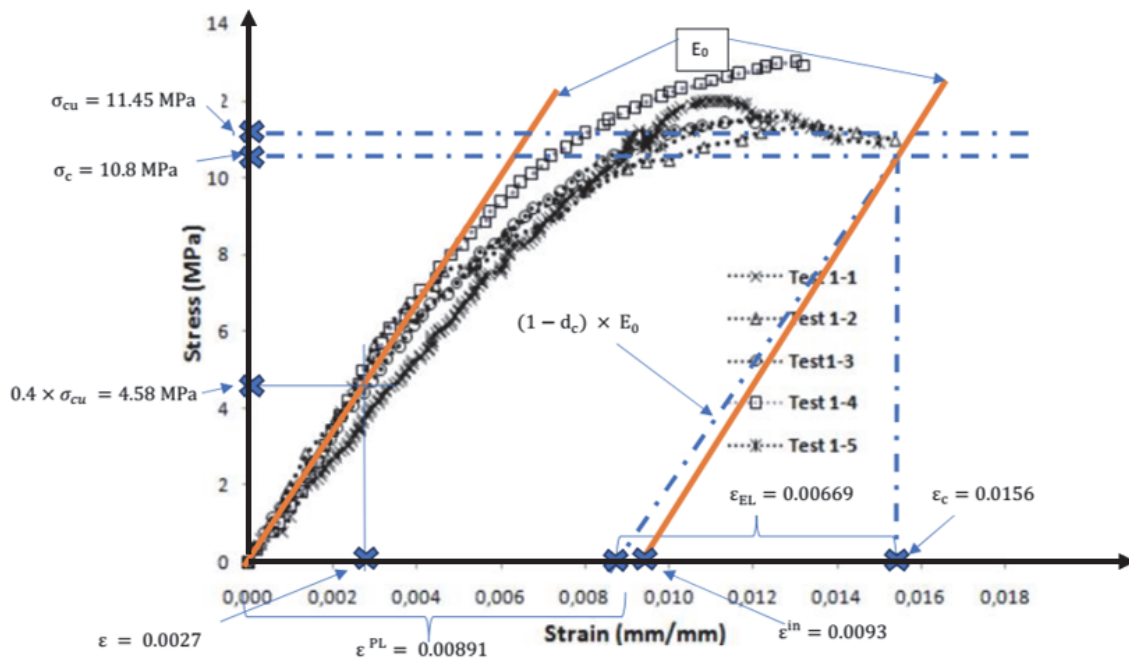
Figure 13: The stress-strain curve of compressed earth block solicited to a uniaxial load in compression.
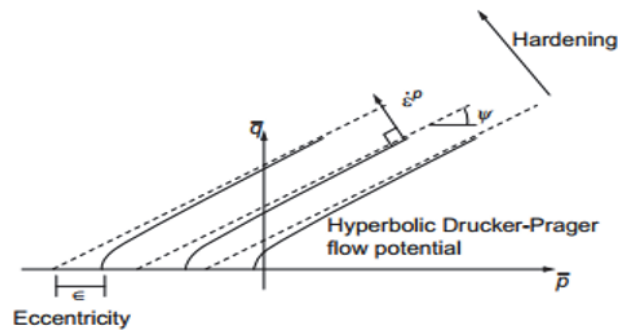
Figure 14: (Dilation angle) Drucker-Prager hyperbolic potential function in the meridional plane [21].

For soils, the angle of dilatancy ψ is often correlated with the angle of internal friction φ (Hughes et al., 1977; Bolton, 1986; Vaidt Sasitharan, 1992). Dano, (2001) adopts the following correlation $\psi = \varphi - 30°$, which is representative of many soils ([21],[22]). For our case, the building material is non-cohesive soil with a friction angle of $\varphi = 35°$ (Fig. 5). Therefore, the proposed expansion angle for the study is:

$$\psi = \varphi - 30° = 35° - 30° = 5° \tag{15}$$

The eccentricity E is the rate that leaves the hyperbolic plastic potential function approaching the asymptote at the uniaxial tensile stress. The dilation angle increases rapidly at lower confining stress when an eccentricity is large, as shown in Fig. 14.

The role of eccentricity is to provide the rate at which the asymptote of the plastic potential function is evaluated, and the expansion angle indicates the volume change caused by the confining stress in the material. It is used to describe the flow rule, which is derived from the no associated flow rule. According to [21], the default value of eccentricity is $E = 0.1$.

A soil submitted to vertical stress tends to deform in the horizontal direction. However, as a soil element is confined by neighbouring soil elements, its horizontal deformation is limited by the development of horizontal stress. The value of the horizontal stress depends on the capacity of the soil to deform, and thus on the type of soil. In a homogeneous soil block

with a horizontal surface, the lateral pressure coefficient (K_0) is the ratio between the horizontal effective stress σ_{0h}, and the vertical effective stress σ_{0v} [21]:

$$K_0 = \frac{\sigma_{0h}}{\sigma_{0v}} \tag{16}$$

The K_0 coefficient can be measured using a triaxial apparatus or a specific odometer cell. For soils, Jaky [23] studied the stability of a block with the Mohr-Coulomb criterion and he determined the value of the K_0:

$$K_0 = 1 - \cos(\varphi) \tag{17}$$

where φ is friction angle [23]

For our case, the internal friction angle is $\varphi = 35°$,

$$K_{0,\exp} = 1 - \sin(35°) = 0.42$$
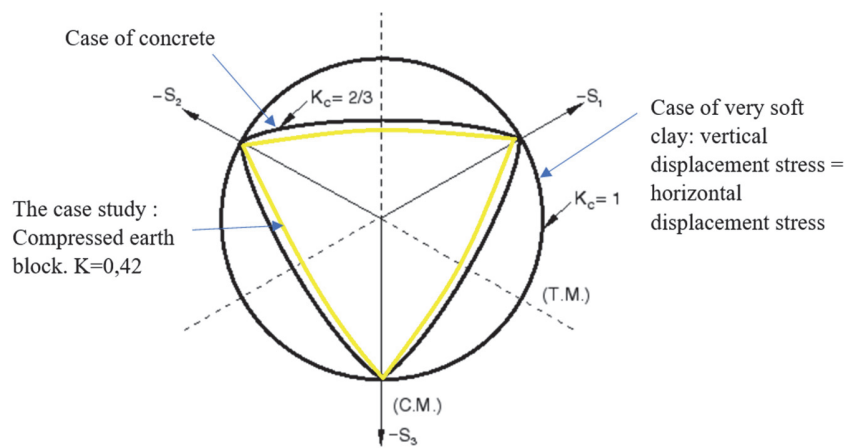
Figure 15: K_0 as a function of the position of the compressed earth block in relation to the other blocks.

In this numerical study of the compressed earth block consisting of homogeneous soil, the core area of the compressed earth block is the area most condemned by the neighbouring soil elements. Then, we are interested in the study of the lateral pressure coefficient at the central node N 1 in Fig. 16.

Fig. 17 shows the distribution of stresses in the function of time in the nodal element N1. We can notice that the stresses S_{12}, S_{13}, and S_{23} are almost negligible compared to the rest of the stresses. Adding to that, constraint S_{22} is linear and presents the maximum values. Thus, the constraints S_{33} and S_{11} have the same values in the function of time. So, we just discuss S_{11} as a function of S_{22} to calculate the lateral pressure coefficient.

Fig. 18 represents the stress S_{11} as a function of the stress S_{22}. It also presents a linear regression of the curve S_{11} in the function of S_{22}, which is $S_{11} = 0.0863 \times S_{22}$ with a coefficient of determination $R^2 = 0.9934$ and a correlation coefficient $R = 0.9968511$. Then, the positive linear relationship between the variables is strong.

The friction angle for our simulation is:

We have

$$K_{0,sim} = 1 - \sin(\varphi_{sim}) \text{ [23]} \tag{18}$$

Therefore

$$\varphi_{sim} = \arcsin(1 - K_{0,sim}) \tag{19}$$

$$\varphi_{sim} = \arcsin(1 - 0.0863) = 66.02°$$
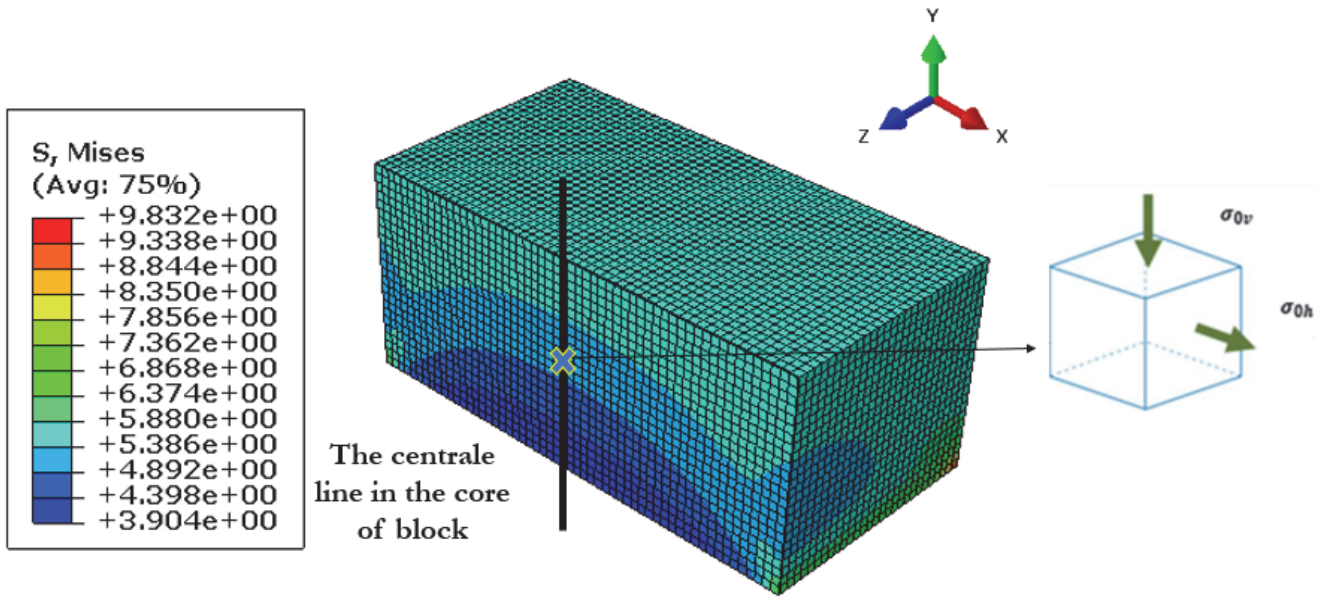
Figure 16: The intermediate relation between the vertical and horizontal stresses of N 1: Central node at the core of the compressed earth block located at depth Y=H/2.
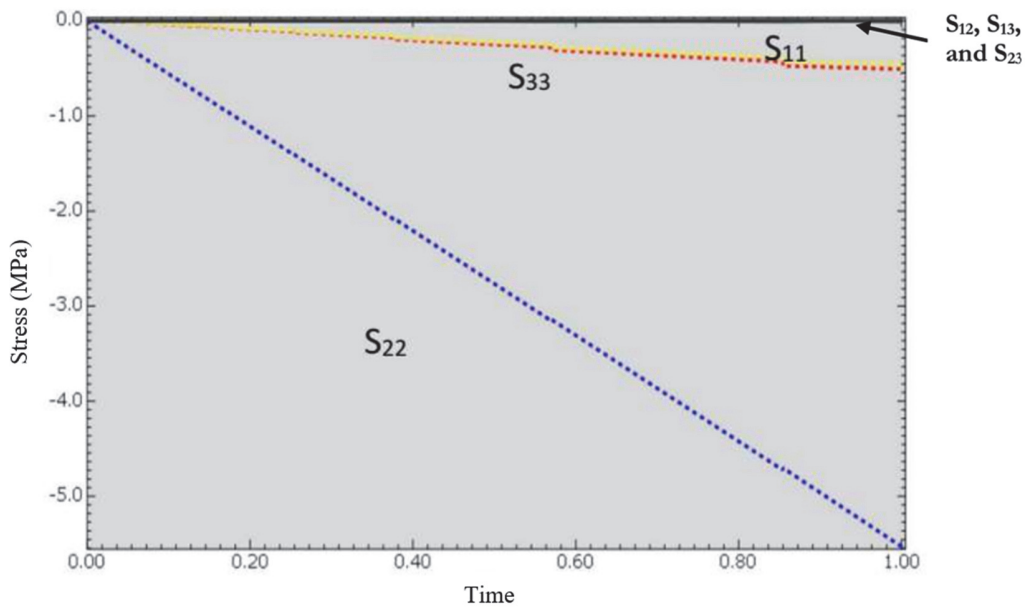
Figure 17: the distribution of S_{11}, S_{22}, S_{33}, S_{12}, S_{13}, and S_{23} as a function of time.

We notice that there is a difference between the experimental and simulation values of the lateral pressure coefficient and the friction angle; for the experiment, the distribution of the layers of the soil in the block is less homogeneous compared to the simulation which presents the layers of soil as ideally homogeneous isotropic.

Biaxial tests, applying force in the planar directions, allow researchers to find the appropriate material at the correct quantity without loss of quality in their products [24].

In reality, composite materials are often submitted to complex loads in which one or two three-dimensional stress states exist. For effective composite design, tests must represent these real loading conditions. When a block is tested biaxially, four perpendicular forces are applied to the specimen.
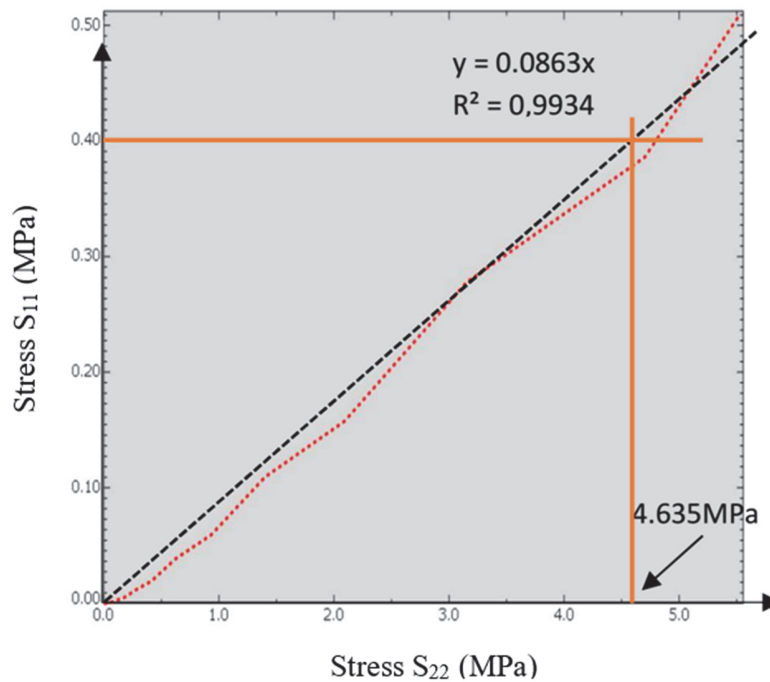
Figure 18: S_{11} in function S_{22}.

The objectives behind the execution of the biaxial test will be presented briefly, namely biaxial tests are not only used to validate the rupture criterion. Rashedi et al [25] presented another objective of applying biaxial tests is the study of crack. In addition, biaxial tests are an interesting way to identify material properties by doing a single test instead of several uniaxial tests [26].

According to the work of Wastiels [27], the ratio of the initial equibiaxial compressive yield strength and the initial uniaxial compressive yield strength is:

$$\frac{\sigma_{bc}}{\sigma_c} = 1.16 \text{ is the default value.} \tag{20}$$

Compressive strength is the most important performance for earthen constructions, and it is the one that will determine the architectural choices. However, in a thorough approach to the behavior of the structures, it is necessary to know the tensile behavior. In addition, earthen structures are also stressed in tension and shear in the case of strong wind, seismic events, point loading, and differential settlement in the foundations [28].

The tensile behavior of the earth block can be modeled using different approaches. The total deformation crack model is based on rupture energy functions. These functions are related to the width of the crack band. For our case, we used the concept of total deformation, which is related to a mixed linear-nonlinear behavior [29]. Eqns. 21, 22 and 23 are based on the relationship described below.

Ben Ayed et al [1] focused their study on the behavior of blocks under the action of simple compression stress.

In addition, our work of numerical simulation of the rupture behavior of the studied block requires us to define the tensile behavior of the study material. However, when we want to test the block experimentally in a direct tensile test, we will be faced with a poorly constructed experience, since we cannot maintain the block at the extremities. Parker et al [30] recommended testing the tensile strength of brittle blocks indirectly or to use the analytical models presented in the literature.

The " tensile stiffening " model (21) is consistent with the assumptions cited by Ben Ayed et al [1]. It represents a brittle behavior in tensile stress. Martins et al [31] split the " tensile stiffening " model into 3 phases. The first is shown by the linearity of the elastic region. The second phase is initiated by the initial cracking of the block and a reduction in the stiffness of the block. In the last phase, the block tends to the failure phase; there is a stable cracking with the opening of the existing cracks.

$$f_c = \left(\begin{array}{ll} E \times \varepsilon & \varepsilon \leq \varepsilon_{cr} \\ \dfrac{f_t^{'}}{1 + \sqrt{(200 \times \varepsilon}} & \varepsilon > \varepsilon_{cr} \end{array} \right) \qquad (21)$$

with

$$f_t^{'} = 0.33\sqrt{f_c^{'}} \, MPa \, [29] \qquad (22)$$

and f'_c : ultimate compressive strength.
Therefore

$$f_t^{'} = 0.33\sqrt{11.45} = 1.116 MPa$$

and

$$\varepsilon_{rc} = \frac{f_t^{'}}{E_c} \text{ according to (Fig. 19)} \qquad (23)$$

Then

$$\varepsilon_{rc} = \frac{1.116}{1696.29} = 0.000658$$
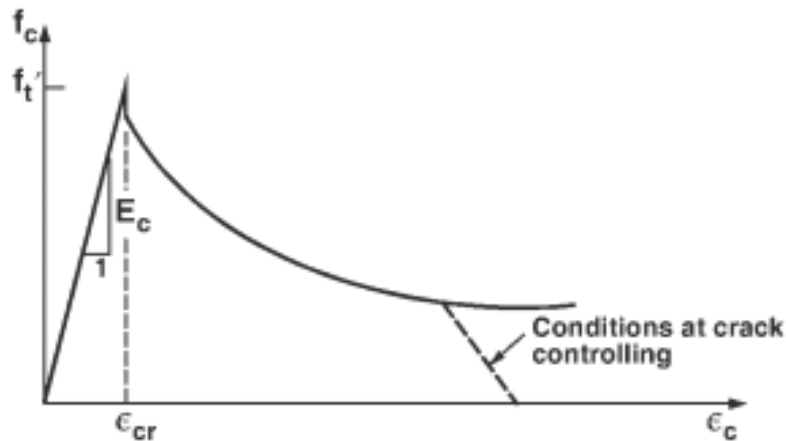
Figure 19: The curve of the stress-strain function (tensile stiffening) [29].

To understand the interaction forces between the solidified grains in the block, the apparent viscosity was introduced to characterize the strength of the solidified grains in the moving block. In addition, the decrease in solid viscosity generally indicates an increased adhesion property of the grains [32]. For our case, the compressed earth block undergoes compression in the manufacturing phase, which decreases the viscous state of the grains. This means that the cohesive forces caused by surface sintering and particle melting increase, which can lead to agglomerated and bonded grains, while non-zero viscosity suggests that the solidified grains in the block have no bonding ability [32]. Furthermore, W. Hong, [21] proposes that a zero value of viscosity is suggested as an input for the mechanical parameters of solids in ABAQUS. Then a proposal of 0 Pa.s value of viscosity is accepted for compressed earth blocks.
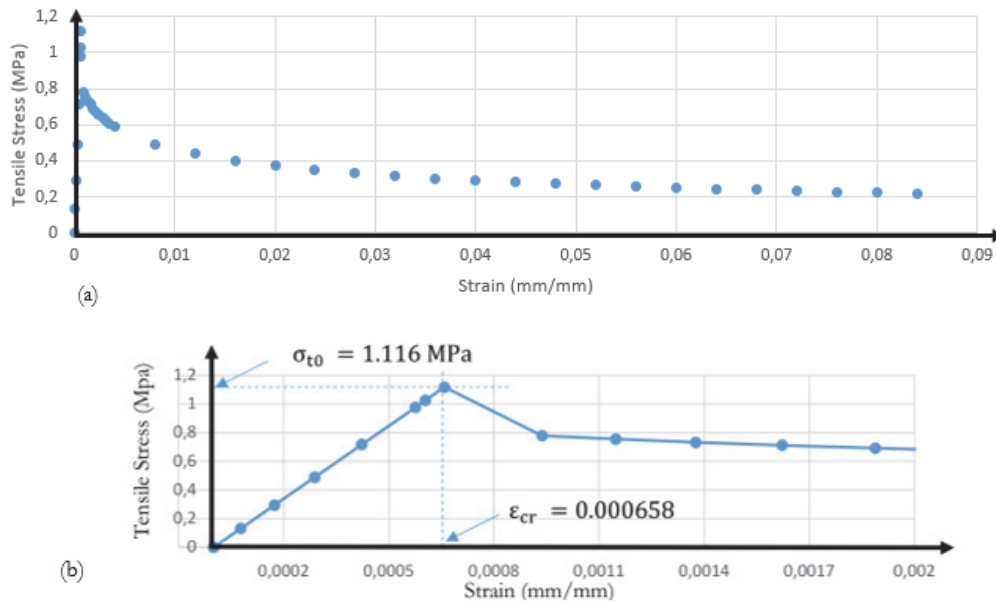
Figure 20: Stress-strain curve in tensile testing, (a) Theoretical curve, (b) Theoretical curve zoomed in interval [0, 0.002].

UNIAXIAL TEST IN "SIMPLE COMPRESSION" SIMULATION

Brittle ruptures are due to the initiation and subsequent growth of cracks from pre-existing defects. Therefore, knowledge of 3-D crack growth under different loading conditions (mainly in the stress field) is necessary to understand the macroscopic constitutive behavior of masonries [33]. The crack initiation is mainly expected to follow in the direction parallel to the maximum compressive load [34]. This is also suggested by Lajtai (1971, 1974) who shows that using brittle material specimens, cracks initiate at points of maximum tensile stress and propagate along a curvilinear direction that becomes approximately parallel to the compression field [35]. This paragraph examines the crack propagation of a solid block by ABAQUS, adopting the experimental results of Ben Ayed et al [1] as data to be input into the numerical computation.

The numerical simulation of the experimental test of compressed earth blocks in single compression test 1-5 (Fig. 13) was achieved by using ABAQUS. The compressed earth block is manipulated numerically within the framework of a macro-modeling strategy. It is, therefore, treated as a homogeneous solid and no distinction was made between the manufacturing elements. The mesh adopted for the finite elements was chosen according to the qualitative studies pre-selected in Figs. 6 and 7. This mesh uses a total number of nodes: 86925 and a total number of elements: 80640 with a mesh: linear hexahedron of type C3D8R. The choice of this mesh refines better the crack propagation. The block was modelled using the plastic material model defined in this work. Thus, the simulation needs to have the inelastic parameters of the material. These values have been calculated in Tabs. 2 and 3.

$$\varepsilon_{c,j}^{in} = \varepsilon_{c,j} - \frac{\sigma_{c,j}}{E_0} \tag{24}$$

with

$\sigma_{c,j}$:The compressive stress at point j;

$\varepsilon_{c,j}$:The compressive strain at point j;

E_0 :Young's modulus.

Tab. 2b illustrates the value of the damage compressive stresses. In the softening phase starting from the inelastic deformation equivalent to the ultimate stress is equal to the value of Eqn. (25).

$$d_{c,j} = 1 - \frac{\sigma_{c,j}}{\sigma_{u,c}} \tag{25}$$

Inelastic deformation in compression	The compressive stress	Inelastic deformation in compression	The compressive stress
0	[0; 4.58]	0.003166384	10.35
0.0000465193	5.25	0.00346781	10.45
0.0000826603	5.8	0.00373976	10.6
0.00020723	6.2	0.004041185	10.7
0.000272847	6.7	0.004342611	10.8
0.000456368	7	0.004644037	10.9
0.000610413	7.35	0.004945463	11
0.000705507	7.8	0.005246889	11.1
0.000830076	8.2	0.005548314	11.2
0.000925169	8.65	0.005820264	11.35
0.001138167	8.9	0.006136428	11.425
0.001262736	9.3	0.006482068	11.45
0.00150521	9.5	0.006871922	11.4
0.001806635	9.6	0.007291252	11.3
0.002049109	9.8	0.007710582	11.2
0.002350535	9.9	0.008129913	11.1
0.002563532	10.15	0.008549243	11
0.002864958	10.25	0.008968573	10.9

Table 2a: The inelastic deformation in compression of a solid block.

Compressive damage	Inelastic deformation in compression	Compressive damage	Inelastic deformation in compression
0	[0; 0.006482]	0.030567686	0.008129913
0.004366812	0.006871922	0.03930131	0.008549243
0.013100437	0.007291252	0.048034934	0.008968573
0.021834061	0.007710582	0.056768559	0.009233164

Table 2b: The compression damage parameter of a solid block.

Tab. 2a shows the elastic phase of material. The inelastic deformation is equal to 0, and in the plastic phase, the inelastic deformation is equal to the value of Eqn. (24).

Inelastic deformation in traction	Tensile stress MPa	Inelastic deformation in traction	Tensile stress MPa
0	1.11664900	0.0237936	0.3499490
0.0004783	0.77920212	0.0278044	0.3317010
0.0007020	0.75500643	0.0318135	0.3163471
0.0009436	0.73247168	0.03582127	0.30316688
0.0012032	0.71138914	0.03982805	0.29167304
0.0014809	0.69159390	0.04383403	0.28152144
0.0017768	0.67295144	0.04783937	0.27246062
0.0020910	0.65534989	0.05184418	0.26430168
0.0024234	0.63869410	0.05584855	0.25689934
0.0027742	0.62290237	0.05985253	0.25013969
0.0031435	0.60790342	0.06385619	0.24393185
0.0036525	0.58943886	0.06785957	0.23820230
0.0077093	0.49302112	0.07186270	0.23289074
0.0117417	0.43804013	0.07586562	0.22794720
0.0157639	0.40039702	0.07986834	0.22332980
0.0197805	0.3722163	0.083870893	0.21900316

Table 3a: The inelastic tensile deformation of a solid block.

Tab. 3a presents the inelastic tensile deformation of a solid block. In the elastic phase of the material, the inelastic tensile strain is equal to 0 and in the plastic phase, the inelastic tensile strain is equal to the value of Eqn. (26).

$$\varepsilon_{t,j}^{in} = \varepsilon_{t,j} - \frac{\sigma_{t,j}}{E_0} \tag{26}$$

with:

$\sigma_{t,j}$: The tensile stress at point j;

$\varepsilon_{t,j}$: The tensile strain at point j;

Tensile damage	Inelastic strain in traction	Tensile damage	Inelastic strain in traction
0	0	0.686607834	0.023793697
0.302196	0.000478	0.702949584	0.027804455
0.3238641	0.000702	0.716699606	0.031813506
0.3440448	0.000943	0.728502972	0.035821276
0.362925	0.001203	0.738796125	0.039828052
0.3806523	0.00148	0.747887257	0.043834037
0.3973473	0.001776	0.756001549	0.047839379
0.4131102	0.002091	0.763308181	0.051844188
0.428026	0.002423	0.769937244	0.055848552
0.4421681	0.002774	0.775990762	0.059852537
0.4556002	0.003143	0.781550105	0.063856197
0.4721359	0.003652	0.786681128	0.067859575
0.5584815	0.007709	0.79143782	0.0718627
0.60771904	0.0117417	0.79586494	0.07586562
0.64142982	0.015763957	0.8	0.07986834
0.66666666	0.01978057	0.80387466	0.08387089

Table 3b: The damage parameter of the traction of a solid block.

The damage parameter of the traction of a solid block is illustrated in Tab. 3-b. The tensile damage is equal to:

$$d_{t,j} = 1 - \frac{\sigma_{t,j}}{\sigma_{u,t}} \tag{27}$$

with

$\sigma_{u,t}$: is the ultimate tensile stress;

$\sigma_{t,j}$: the tensile stress at point j.

The initial and boundary conditions provided were chosen to adequately simulate the test configuration and reduce the number of computational iterations:

In Fig. 21, the block is condemned between two plates. This condition is modelled by two initial conditions; namely: face 1 below the block has an embedded bond and face 2 above undergoes a concentric force and reaches a value $F_{max} = 3 \times 10^5 N$, this is equivalent to a pressure:

$$P_{max} = \frac{F_{max}}{240 \times 220} = 5.68 MPa$$

Face 2 moves vertically to a maximum value of:

$$\Delta l_{max} = \varepsilon_{c,r} \times h \tag{28}$$

The indices $\varepsilon_{c,r}$ is the strain at compressive rupture stress and h is the block height.

This gives $\Delta l_{max} = 0.0156 \times 97 = 1.513 mm$. Therefore, a choice of maximum displacement along the Y-axis of face 2 greater than Δl_{max} is required to have the block damage. For our case, we choose 2 mm to facilitate the computational iteration.
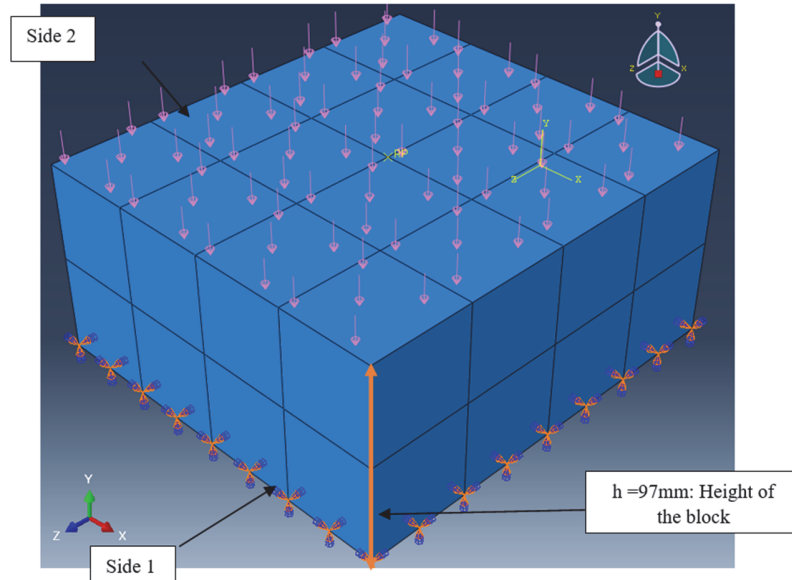
Figure 21: Initial and boundary conditions for the simulation of damage in compression test of the solid block.

The analysis of the results obtained from the crack propagation presented in Fig. 22 is similar to the qualitative study in the experimental test (Fig. 3a) presented in the article [1].

Fig. 22a illustrates the concentration of stress in traction. These solicitations will damage the block, and it will deteriorate following a linear propagation. The crack begins from the extremities of support below the application of the vertical force and it spreads vertically towards the other extremities; this remark is well illustrated in the case of the solicitations of damage in compression. The crack in Fig. 22b follows the same trajectory that it illustrates the block in damage in traction. The cohesion of the block during the simple compression test is discussed in Figs. 22c and 22d. These figures present the maximum deformation of the block. We notice a maximum displacement of the elements following the same path in Figs. 3a, 22a, and 22b. Thus, the maximum displacement amplitudes in Fig. 22g and the uniaxial displacement U22 in Fig. 22h of the finite elements in the block show a similarity of this linear and moustachial crack propagation.

It can be seen, from the distribution of the von-Mises stresses in Fig. 22e and the vertical stress S22 in Fig. 22f that the propagation of the cracks starts from the most stressed zones in the combined compression and tension test, i.e. the sharp corners in contact (block & lower plate), they progress to the extremity at the top (practically parallel to the vertical pressure force along the Y-axis) or almost horizontally, the cracks cross each other giving a moustached shape.

Fig. 23a shows a vertical compression test to rupture, the failure of this block is a crack that is parallel to the direction of the compression load (Fig. 23b). Ben Ayed et al [1] assumed that the material is isotropic and homogeneous. they implemented the parameters (Young's modulus $E = 1700 MPa$, Poisson's ratio $\nu = 0.2$) as elastic properties of the predefined material. Thus, Ben Ayed et al [1] determined two other parameters of block failure in a single compression: cohesion coefficient $c = 781.43 MPa$ and φ internal friction angle $\varphi = 35°$.

Fig. 24 shows the uniaxial compression force as a function of the vertical displacement of the block. This curve indicates an ultimate force $P_{max} = 0.6 MN$. The slope (A5%) intersects with the curve at $P_{5\%} = 0.6 MN$, this value is the maximum force PQ which lies between the two slopes A and A5%. Therefore, the type of failure of the stressed block is mode 1 [36,37].

The non-linear behaviour in the plastic zone around the crack front is verified by the inequality (29) [36].

$$\frac{P_{max}}{P_Q} > 1.10 \qquad (29)$$
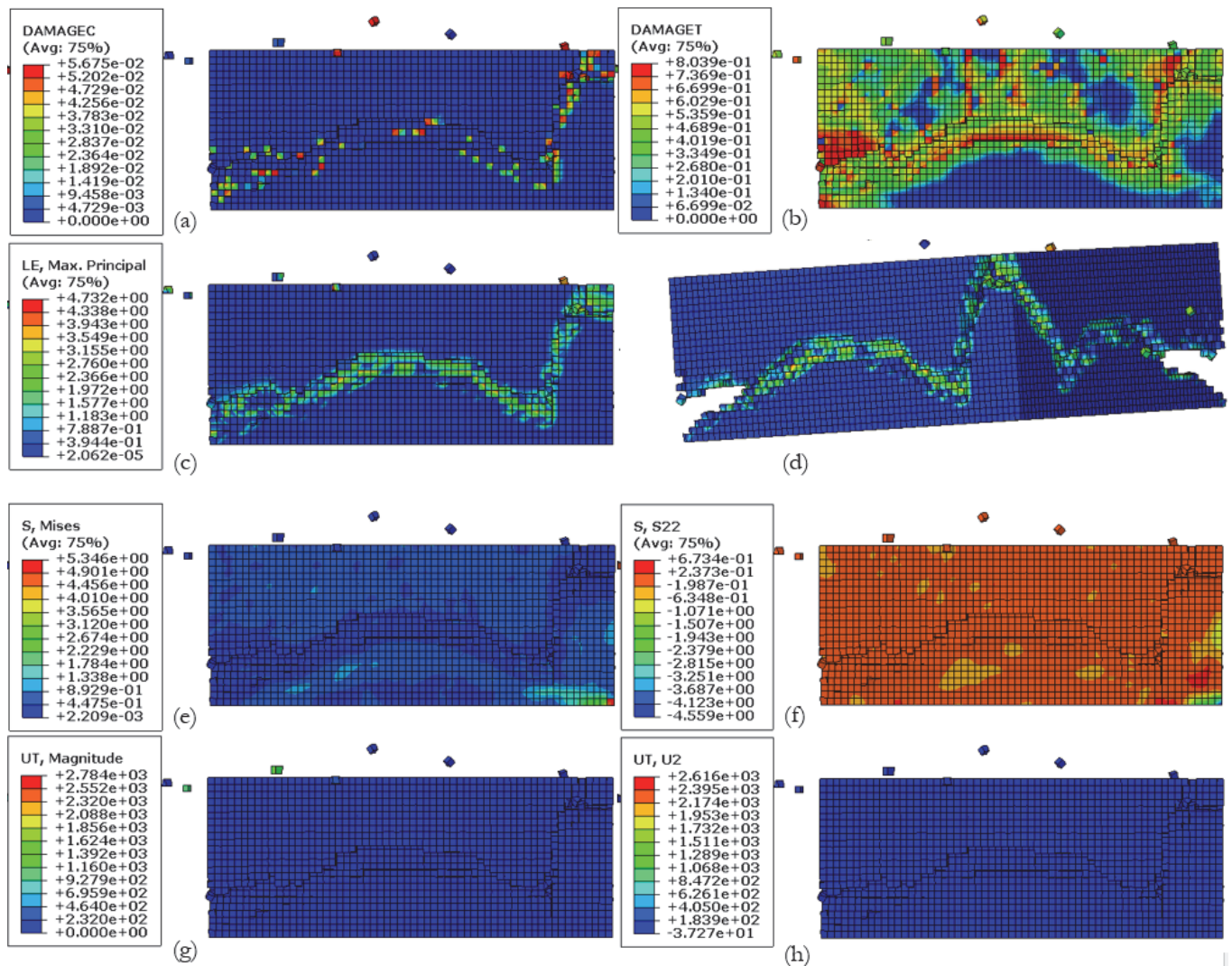
Figure 22: The crack propagation in numerical simulation in case of: ((22-a): compressive damage; (22-b): tensile damage; (22-c and 22-d): maximum elastic strain; (22-e): the von-Mises stress; (22-f): the S_{22} stress; (22-g): maximum magnitude displacements; (22-h): maximum uniaxial U_{T2} displacements.
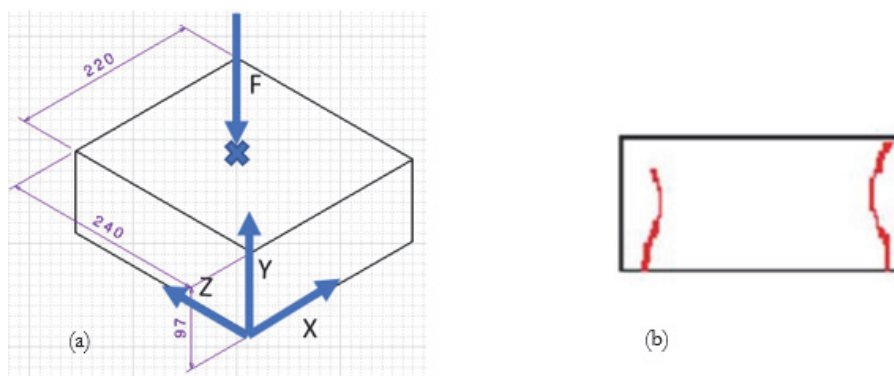
Figure 23: the concentric force applied to a single block of compressed earth.
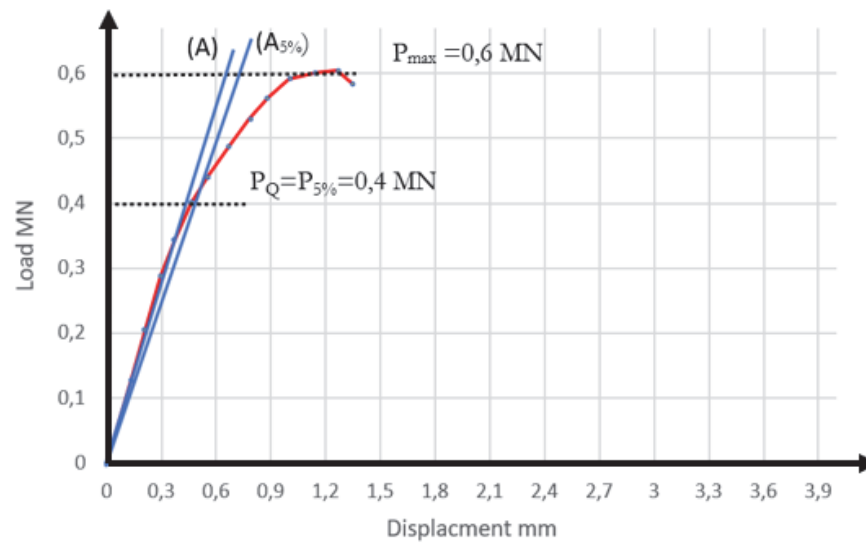
Figure 24: load-displacement records of a compressive test.

The cracks evolve over the time, and this is due to a weakness of the masonry at the supports when the stress is increased. Numerical visualization of this rupture process is particularly an important issue when dealing with the compressive strength of compressed earth block structures; particularly, the crack propagation of damaged structures should be eliminated in the design stage beforehand.

CONCLUSION

This paper is based on a numerical study of the mechanical behavior of a solid block of compressed earth. In the first step, we addressed a mixed methodological study that is founded on the experimental results developed by Ben Ayed et al [1] and our numerical simulation by the ABAQUS code. In this part, we detailed the mechanical properties in the elastic behavior of the block. In addition, we have illustrated that macro-cracks can be generated predictively in the corners of the block and propagated almost vertically towards the ceiling; this suggestion is based on the maximum deformations of the finite elements which constitute the numerical model. They move horizontally concerning a centre of rotation presenting the point of concentration of the von-Mises stress. A validation of our numerical model in the elastic part with the experiment [1] is accorded. In turn, the finite elements of the numerical model were subjected to a dominant stress S_{22} about the other stresses, which will be neglected in the following studies. In the second step, we proposed a mathematical model of the mechanical characteristics of damage at the rupture in compression. The inelastic parameters of the selected solid block were presented, for example: dilatation angle, eccentricity, lateral pressure coefficient, inelastic deformation in compression, and inelastic deformation in tension. Finally, we simulated the crack propagation. This last part illustrates the 3D defects visualized in the numerical simulation of the block up to rupture. Indeed, we presented images of the propagation, according to several criteria of cracks that start from corners and cross each other horizontally and/or propagate towards the ceiling of the block in a way that is practically parallel to the application of the force of the compression test. A comparison of the simulation and the experimental images shows a good resemblance.

REFERENCES

[1] Ben Ayed, H., Limam, O., Aidi, M. and Jelidi A. (2016). Experimental and numerical study of Interlocking Stabilized Earth Blocks mechanical behavior, J. Journal of Building Engineering, 7, pp. 207-216.
DOI: 10.1016/j.jobe.2016.06.012.

[2] Kulshreshtha, Y., Mota, N., Jagadish, K., Breadboard, J., Vardon, P., van Loosdrecht, M. and Jonkers, H. (2020). The potential and current status of earthen material for low-cost housing in rural India, J. Construction and Building Materials, 247. DOI: 10.1016/j.conbuildmat.2020.118615.
Pacheco-Torgal, F. and Jalali, S. (2012). Earth construction: Lessons from the past for future eco-efficient construction, J. Construction and Building Materials, 29, pp. 512-519. DOI: 10.1016/j.conbuildmat.2011.10.054.

[3] Schroeder, H. (2016). Chapter 3: Earth Building Materials – Production, Requirements, and Testing, Sustainable Building with Earth, pp. 11-154, Springer International Publishing.

[4] Egenti, C., Khatib, J.M. and Oloke, D. (2014), Conceptualisation and pilot study of shelled compressed earth block for sustainable housing in Nigeria, J. International Journal of Sustainable Built Environment, 3(1), pp 72–86. DOI: 10.1016/j.ijsbe.2014.05.002.

[5] Giuffrida, G., Caponetto, R. and Cuomo1, M. (2019). An overview on contemporary rammed earth buildings: technological advances in production, construction, and material characterization. IOP Conference Series: Earth and Environmental Science, 296, SBE19 - Resilient Built Environment for Sustainable Mediterranean Countries, Milan, Italy. DOI: 10.1088/1755-1315/296/1/012018.

[6] Winterkorn, H.F. and Pamukcu, S. (1991). Soil Stabilization and Grouting. In: Fang HY. (eds) Foundation Engineering Handbook. Springer, Boston, MA. DOI: 10.1007/978-1-4757-5271-7_9.

[7] Uzoegbo, H. C. (2016). Dry-stack and compressed stabilised earth-block construction. J. Nonconventional and Vernacular Construction Materials, pp. 205–249. DOI: 10.1016/B978-0-08-100038-0.00008-1.

[8] Islam, M. S., Elahi, T. E., Shahriar, A. R. and Mumtaz, N. (2020). Effectiveness of fly ash and cement for compressed stabilized earth block construction, J. Construction and Building Materials, 255.
DOI: 10.1016/j.conbuildmat.2020.119392.

[9] Ruiz, G., Zhang, X., Edris, W., Cañas, I. and Garijo, L. (2018). A comprehensive study of mechanical properties of compressed earth blocks, J. Construction and Building Materials, 176, pp. 566-572.
DOI: 10.1016/j.conbuildmat.2018.05.077.

[10] Guillaud, H., Joffry, T. oudul, P. and CRAterre-EAG. (1995). Manuel de conception et de construction « Blocs de terre comprimée », Deutsches Zentrum für Entwicklungstechnologien – GATE, ISBN 3-528-02082-2.

[11] Guanqi, L., Yihong, W., Guiyuan, Z. and Jianxiong, Z. (2020), Compressive strength of earth block masonry: Estimation based on neural networks and adaptive network-based fuzzy inference system, J. Composite Structures, 235. DOI: 10.1016/j.compstruct.2019.111731.

[12] Illampas, R., Ioannou, I. and Charmpis, D. C. (2011). A study of the mechanical behaviour of adobe masonry, J. Structural Repairs and Maintenance of Heritage Architecture XII, 118, pp 485 – 496. DOI: 10.2495/STR110401.

[13] DS SIMULIA. (2022). ABAQUS, Version 6.6.

[14] Venkatarama Reddy, B.V. (2012). 13 - Stabilised soil blocks for structural masonry in earth construction, J. Modern Earth Buildings, pp. 324-363. DOI: 10.1533/9780857096166.3.324.

[15] Ben Mansour, M., Jelidi, A., Cherif, A. and Jaballah, S. B. (2016). Optimizing thermal and mechanical performance of compressed earth blocks (CEB), J. Construction and Building Materials, 104, pp. 44-51.
DOI: 10.1016/j.conbuildmat.2015.12.024.

[16] Hashim, D.T., Hejazi F. and Lei, V.Y. (2020). Simplified Constitutive and Damage Plasticity Models for UHPFRC with Different Types of Fiber, J. International Journal of Concrete Structures and Materials.
DOI: 10.1186/s40069-020-00418-9.

[17] Grassl, P., Xenos, D., Nyström, U., Rempling, R. and Gylltoft, K.2013, CDPM2: A damage-plasticity approach to modelling the failure of concrete, J. International Journal of Solids and Structures, 50(24), pp. 3805-3816.
DOI: 10.1016/j.ijsolstr.2013.07.008.

[18] Birtel, V. and Mark P. (2006). Parameterised Finite Element Modelling of RC Beam Shear Rupture, ABAQUS Users' Conference at Ruhr-University Bochum, Universitätsstr. 150, 44780 Bochum, Germany Institute for Reinforced and Prestressed Concrete Structures.

[19] Terzaghi, K., Peck, R. B. and Mesri, G. (1996). Soil Mechanics in Engineering Practice, 3rd Edition ,John Wiley & Sons, INC. ISBN: 978-0-471-08658-1.

[20] Hong, W. (2020). Chapter 3 - The investigation of the structural performance of the hybrid composite precast frames with mechanical joints based on nonlinear finite element analysis, Woodhead Publishing Series in Civil and Structural Engineering - Hybrid Composite Precast Systems, pp. 89-177. DOI: 10.1016/B978-0-08-102721-9.00003-0.

[21] Dano, C., Hicher, P., Tailliez S. and Varjabédian, M. (2002). Identification des paramètres de comportement des sols injectés par analyse inverse d'essais pressiométriques, J. Revue Française de Génie Civil, pp. 631-660.
DOI: 10.1080/12795119.2002.9692392.

[22] MESTAT, P. (1998). Etat de contraintes initiales dans les sols et calcul par éléments finis, le Bulletin Des Laboratoires Des Ponts Et Chaussées – 215, RÉF : 4188, pp. 15-32.

[23] Yuan, R., Zhenpeng, Y., Qiao, H. and Zheng, R. (2018). Constitutive model and rupture criterions for lightweight aggregate concrete: A true triaxial experimental test, J. Construction and Building Materials, 171, pp. 759-769. DOI: 10.1016/j.conbuildmat.2018.03.219.

[24] Rashedi, A., Sridhar, I. and Tseng, K.J. (2016). Rupture characterization of glass fiber composite laminate under experimental biaxial loading, J. Composite Structures, 138, pp. 17-29. DOI: 1016/j.compstruct.2015.11.029.

[25] Hemelrijck, D. V., Makris, A., Ramault, C., Lamkanfi, E., Paepegem, W V. and Lecompte, D. (2008). Biaxial testing of fibre-reinforced composite laminates. J. Proceedings of the Institution of Mechanical Engineers, Part L: Journal of Materials: Design and Applications, 222(4), pp. 231-539. DOI: 10.1243/14644207JMDA199.

[26] Wastiels, J. (1979). Rupture criteria for concrete under multiaxial stress states,ETH Zürich-Section : Session I : Équations constitutives - critères de rendement, Tome. 29. DOI: 10.5169/seals-23527.

[27] Pkla, A., Mesbah, A. and Rigassi V. (2003). Comparaison de méthodes d'essais de mesures des caractéristiques mécaniques des mortiers de terre, J. Materials and Structures, 36, pp. 108–117. DOI : 10.1007/BF02479524.

[28] Selby, R. G. and Vecchio, F. J. (1997), A constitutive model for analysis of reinforced concrete solids. J. Canadian Journal of Civil Engineering, pp. 460–470. DOI: 10.1139/l96-135.

[29] Parker, C. K., Tanner, J. E. and Varela, J. L. (2007). Evaluation of ASTM Methods to Determine Splitting Tensile Strength in Concrete, Masonry, and Autoclaved Aerated Concrete. J. Journal of ASTM International, 4(2), JAI100446.

[30] Martins, M. P., Rangel, C. S., Amario, M., Lima, J. M. F., Lima, P. R. L. and Toledo Filho, R. D. (2020). Modelling of tension stiffening effect in reinforced recycled concrete, J. IBRACON Estrut. Mater, 13(6), e13605. DOI: 10.1590/S1983-41952020000600005.

[31] Yanling, Z., Zhuoqing, A., Hao, B., Qi, L. and Zhancheng, G. (2015). Characterization and measurement of apparent viscosity of solid particles in fixed beds under high temperature, J. Powder Technology, 284, pp. 279-288. DOI: 1016/j.powtec.2015.06.069.

[32] Hongyu, W., Arcady, D. and Elena, P. (2019). Comparative analysis of mechanisms of 3-D brittle crack growth in compression, J. Engineering Rupture Mechanics, 220. DOI: 10.1016/j.engfracmech.2019.106656.

[33] Hadi, H., Kourosh, S., Marji, M. F. and Moarefvand, P. (2014). Experimental and numerical study of crack propagation and coalescence in pre-cracked rock-like disks, J. International Journal of Rock Mechanics and Mining Sciences, 67, pp. 20-28. DOI: 10.1016/j.ijrmms.2014.01.008.

[34] Jun, X., Zheyuan, Z., Xiaochun, X. and Zhaoxia, L. (2018). Crack propagation and coalescence due to dual non-penetrating surface flaws and their effect on the strength of rock-like material, Journal of Geophysics and Engineering, 15(3), pp. 938–951.DOI: 10.1088/1742-2140/aaa98.

[35] González-Velázquez, J. L. Mechanical Behavior and Fracture of Engineering Materials. DOI: 10.1007/978-3-030-29241-6.

[36] Wang, F., Pan, B., Shen Y. and Cui W. (2014). On fracture resistance parameter from non-standard fracture test specimens of titanium alloy, J. Ships and Offshore Structures, pp. 177-185. DOI: 10.1080/17445302.2012.741809.